Earth and Planetary Science Letters 568 (2021) 117030

Contents lists available at ScienceDirect

Earth and Planetary Science Letters

www.elsevier.com/locate/epsl

Tropical Atlantic stratification response to late Quaternary precessional forcing

R.A. Nascimento [a,*], I.M. Venancio [a,b], C.M. Chiessi [c], J.M. Ballalai [a], H. Kuhnert [d], H. Johnstone [d], T.P. Santos [a], M. Prange [d], A. Govin [e], S. Crivellari [c], S. Mulitza [d], A.L.S. Albuquerque [a]

[a] Programa de Geociências (Geoquímica), Universidade Federal Fluminense, Niterói, Brazil
[b] Center for Weather Forecasting and Climate Studies (CPTEC), National Institute for Space Research (INPE), Cachoeira Paulista, Brazil
[c] School of Arts, Sciences and Humanities, University of São Paulo, São Paulo, Brazil
[d] MARUM - Center for Marine Environmental Sciences, University of Bremen, Bremen, Germany
[e] Laboratoire des Sciences du Climat et de l'Environnement/Institut Pierre Simon Laplace, CEA-CNRS-UVSQ, Université Paris Saclay, Gif sur Yvette, France

ARTICLE INFO

Article history:
Received 18 August 2020
Received in revised form 19 May 2021
Accepted 27 May 2021
Available online xxxx
Editor: Y. Asmerom

Keywords:
western tropical Atlantic stratification
precession
ITCZ
South Atlantic Subtropical Gyre

ABSTRACT

The upper ocean circulation in the western tropical Atlantic (WTA) is responsible for the northward cross-equatorial heat transport as part of the Atlantic Meridional Overturning Circulation (AMOC). This cross-equatorial transport is influenced by the thermocline circulation and stratification. Although seasonal thermocline stratification in the WTA is precession-driven, the existence of an orbital pacemaker of changes in the entire WTA upper ocean stratification, which comprises the main thermocline, remains elusive. Here, we present a 300 ka-long record of the WTA upper ocean stratification and main thermocline temperature based on oxygen isotopes ($\delta^{18}O$) and Mg/Ca of planktonic foraminifera. Our $\Delta\delta^{18}O$ record between *Globigerinoides ruber* and *Globorotalia truncatulinoides*, representing upper ocean stratification, shows a robust precession pacing, where strong stratification was linked to high summer insolation in the Northern Hemisphere (precession minima). Mg/Ca-based temperatures support that stratification is dominated by changes in thermocline temperature. We present a new mechanism to explain changes in WTA stratification, where during the Northern Hemisphere summer insolation maxima, the Intertropical Convergence Zone shifts northward, developing a negative wind stress curl anomaly in the tropical Atlantic. This, in turn, pulls the main thermocline up and pushes the South Atlantic Subtropical Gyre southwards, increasing the stratification to the north of the gyre. This mechanism is supported by experiments performed with the Community Earth System Model (CESM1.2). Finally, we hypothesize that the precession-driven WTA stratification may affect the cross-equatorial flow into the North Atlantic.

1. Introduction

The tropics play a major role in the Earth's climate system (Berger et al., 2006; Rutherford and D'Hondt, 2000; Mcintyre and Molfino, 1996). In this area, trade winds connect the circulation of the lower atmosphere to that of the ocean surface. The upper ocean circulation in the western tropical Atlantic (WTA) is responsible for the northward-cross-equatorial transport of heat and salt as part of the upper limb of the Atlantic Meridional Overturning Circulation (AMOC) (Zhang et al., 2011; Hazeleger and Drijfhout, 2006; Lumpkin and Speer, 2003). Most of this transport occurs within the thermocline (Schott et al., 2005, 1998). Instrumental data and model experiments suggest that deep-water formation at the high latitudes of the North Atlantic is linked to the water volume transported northwards within the WTA (Zhang et al., 2011; Vellinga and Wu, 2004; Yang, 1999). Venancio et al. (2018) suggested that WTA thermocline stratification, directly influenced by trade wind stress, affects the water transport towards the North Atlantic during millennial-scale North Atlantic cold-events. Meanwhile, Kaiser et al. (2019) recently reported precessional modulated changes in cross-equatorial water transport during the mid-Pleistocene. Therefore, it is plausible that orbital variations in trade winds pattern and WTA upper ocean hydrography have implications for cross-equatorial transport and AMOC strength.

* Corresponding author.
E-mail address: rodrigoan@id.uff.br (R.A Nascimento).

https://doi.org/10.1016/j.epsl.2021.117030
0012-821X/

On orbital timescales, variations in low latitude insolation are primarily driven by precession (Clement et al., 2004; Berger et al., 1993). Precession-forced variability of trade wind zonality has been documented in the tropical Atlantic (Wolff et al., 1999; Mcintyre and Molfino, 1996; Molfino and Mcintyre, 1990; Mcintyre et al., 1989). This was linked to variations in the intensity of the West African monsoon (COHMAP Members, 1988; Mcintyre et al., 1989; Molfino and Mcintyre, 1990; Mcintyre and Molfino, 1996), which in turn is modulated by boreal summer insolation (Skonieczny et al., 2019; Kutzbach and Liu, 1997; Kutzbach and Guetter, 1986; Kutzbach and Otto-Bliesner, 1982). Changes in trade wind zonality control tropical Atlantic stratification by changing the depth of the shallow seasonal thermocline with a precession beat (Venancio et al., 2018; Mcintyre and Molfino, 1996; Molfino and Mcintyre, 1990; Mcintyre et al., 1989). However, the seasonal thermocline comprises only the thin uppermost portion of the main thermocline.

The main thermocline is ventilated at midlatitudes primarily by buoyancy flux and westerlies-driven Ekman pumping (Sprintall and Tomczak, 1993; Luyten et al., 1983a). The amount of water advected towards low latitudes in the main thermocline depends on the strength of the midlatitude westerlies (Luyten et al., 1993b), while the properties of the main thermocline waters are largely influenced by characteristics of the ocean surface in the formation region (Poole and Tomczak, 1999; Sprintall and Tomczak, 1993). Orbitally-driven changes in the Southern Hemisphere westerlies are primarily controlled by obliquity forcing on the meridional temperature gradient at midlatitudes (Timmermann et al., 2014; Mantsis et al., 2014, 2011). Consequently, the obliquity signal imprinted in midlatitudes can be propagated within the main thermocline towards the WTA. However, the existence of an orbital pacemaker of changes in the main thermocline density structure and hence in the WTA upper ocean stratification remains elusive.

To investigate the response of the WTA upper ocean stratification to orbital forcing and its possible implications for the interhemispheric transport of heat and salt, we present a millennial resolution 300 ka-long record of $\Delta\delta^{18}O$ between surface- and deep-dwelling planktonic foraminifera species ($\delta^{18}O_{Globorotalia\ truncatulinoides}$ - $\delta^{18}O_{Globigerinoides\ ruber}$). In addition, we present a record of main thermocline temperatures based on Mg/Ca ratios of *Globorotalia truncatulinoides*, as well as seawater-$\delta^{18}O$ corrected for changes in ice-volume ($\delta^{18}O_{sw\text{-}ivc}$), a proxy for relative changes in main thermocline salinity. Samples come from sediment core GL-1180 collected off eastern Brazil (8° 27'18" S, 33° 32'53" W, 1037 m water depth) (Fig. 1). Our results show that WTA upper ocean stratification is coupled to precession, particularly during periods of high eccentricity. We propose a new mechanism to explain changes in WTA stratification, which is corroborated by results from the Community Earth System Model (CESM1.2). Finally, we hypothesize a connection between WTA stratification and interhemispheric oceanic transport on orbital timescales.

2. Regional setting

Upper ocean circulation in the WTA is marked by the bifurcation of the southern branch of the South Equatorial Current (sSEC). The sSEC bifurcates between 10 and 14°S (Rodrigues et al., 2007), giving rise to the southward flowing Brazil Current and the northward flowing North Brazil Undercurrent (NBUC)/North Brazil Current (NBC) (Fig. 1) (Stramma and England, 1999). The NBUC/NBC are part of the upper limb of the AMOC (Zhang et al., 2011; Hazeleger and Drijfhout, 2006). At ~8°S, sediment core GL-1180 is sensitive to variations in the latitude of the sSEC bifurcation. The sSEC represents the northernmost boundary of the warm and saline South Atlantic Subtropical Gyre (SASG) (Marcello et al., 2018; Rodrigues et al., 2007; Stramma, 1991), which is clearly marked in temperature at 250 m water depth (Fig. 1). North of the SASG, the thermocline is shallow due to equatorial divergence forced by the trade winds pushing waters at the Ekman layer from the equator towards the subtropics. South of the SASG gyre, the westerlies force the Ekman transport in the opposite direction. This convergence pumps warm surface waters downward and pushes the thermocline down, forming a thick upper ocean layer of warm waters, namely the SASG (Fig. 1).

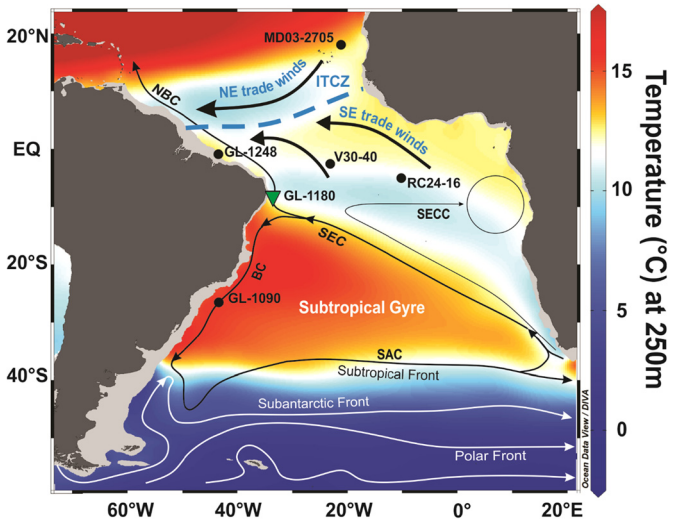

Fig. 1. Location of the sediment core GL-1180 analyzed in this study (green triangle) and other cores used in the discussion (black dots): GL-1090 (Santos et al., 2020; Ballalai et al., 2019; Santos et al., 2017a,b); GL-1248 (Venancio et al., 2018); MD03-2705 (Skonieczny et al., 2019); V30-40 and RC24-16 (Mcintyre et al., 1989);. The color scale depicts annual temperature at 250 m water depth (Locarnini et al., 2013). The dashed blue line represents the average position of the Intertropical Convergence Zone position (ITCZ). Thick black arrows indicate the trade winds. Thin black arrows show the main wind-driven upper ocean circulation. BC: Brazil Current; NBC: North Brazil Current; SAC: South Atlantic Current; SECC: South Equatorial Counter-Current; SEC: South Equatorial Current. White thin arrows represent the Antarctic Circumpolar Current. The figure was generated using the software Ocean Data View (Schlitzer, 2017). (For interpretation of the colors in the figure(s), the reader is referred to the web version of this article.)

The mean sea surface temperature and salinity at site GL-1180 are 27.7°C and 36.3, respectively (Locarnini et al., 2013; Zweng et al., 2013). At 250 m water depth, in the main thermocline, temperature and salinity are 12.1°C and 35.1, respectively (Locarnini et al., 2013). Tropical Water is present in the upper 100 m of the water column, South Atlantic Central Water (SACW) between 100 and 500 m water depth, and Antarctic Intermediate Water from 500 to 1200 m water depth (Stramma and England, 1999). The SACW, the water mass of the South Atlantic main thermocline, is subducted at the South Atlantic Subtropical Front (Stramma and England, 1999; Poole and Tomczak, 1999).

One of the key atmospheric features of the tropics is the Intertropical Convergence Zone (ITCZ), the belt of deep convection located between the Hadley cells of both hemispheres (Schneider et al., 2014). Due to the seasonal asymmetry in the interhemispheric heat budget, the ITCZ migrates southward (northward) during austral summer (winter) (Marshall et al., 2014; Schneider et al., 2014). In the South Atlantic, the SE trade winds and the lower limb of Southern Hemisphere Hadley cell are weaker (stronger) during the austral summer (winter). Furthermore, during austral summer (winter), an anticyclonic atmospheric circulation expands towards the equator in the WTA (Rodrigues et al., 2007). The opposite occurs during austral winter when a cyclonic circulation expands southwards over the continental margin of northeastern Brazil. The variation between atmospheric anticyclonic and cyclonic circulation, and hence positive and negative wind stress curl respectively,

controls the position of the sSEC bifurcation, causing its southward (northward) shift during austral winter (summer) (Rodrigues et al., 2007).

3. Material and methods

3.1. Sediment core GL-1180

We investigate the 1732 cm-long marine sediment core GL-1180 provided by Petrobras. Visual analysis of the core does not indicate any sedimentation disturbance. Sediment samples of approximately 10 cm^3 were taken every 2 cm. For the chemical analyses described below, all sediment samples were wet-sieved to retain the fraction larger than 63 µm. The retained material was dried at 50°C for 24 hours and stored in acrylic flasks. Foraminifera shells were handpicked using a binocular microscope.

3.2. Age model

The age model of GL-1180 is based on six radiocarbon ages (Supporting Information, Table S1) and the visual alignment of the benthic $\delta^{18}O$ record of *Cibicidoides sp.* (see section 3.3) with a global $\delta^{18}O$ stack. For radiocarbon dating, 6 to 10 mg of *Globigerinoides ruber* and *Trilobatus sacculifer* shells were selected from the size fraction larger than 150 µm (Table S1). Analyses were performed at the Beta Analytic Radiocarbon Dating Laboratory (Miami, USA) using accelerator mass spectrometry. Radiocarbon ages were calibrated using the IntCal13 calibration curve (Reimer et al., 2013) with a reservoir effect of 400 ± 200 without additional local reservoir effect. For the benthic $\delta^{18}O$ alignment, the LR04 global $\delta^{18}O$ stack was used (Lisiecki and Raymo, 2005) (Fig. S1 and Table S2 in the Supporting Information). Alignment uncertainties were calculated following Govin et al. (2015). The final age model (Fig. S1) was constructed using the software Bacon v 2.3 (Blaauw and Christen, 2011).

3.3. Isotopic analysis from core GL-1180 and $\Delta\delta^{18}O$ calculation

For isotopic analyses, ten shells of *Cibicidoides sp.* (300-350 µm), *G. ruber* (white, *sensu lato*, 250-300 µm), and *Globorotalia truncatulinoides* (dextral, 300-425 µm) were handpicked. Although *G. truncatulinoides* $\delta^{18}O$ shows a positive correlation with shell size (Birch et al., 2013; Elderfield et al., 2002), $\delta^{18}O$ variation is minimal in shells larger than 250 µm (Birch et al., 2013). The sampling resolution of benthic foraminifera $\delta^{18}O$ was 4 cm (373 samples). The planktonic foraminifera sampling resolution varied between 4 and 2 cm for *G. ruber* and *G. truncatulinoides*, totaling 507 and 509 samples, respectively.

Analyses of $\delta^{18}O$ of benthic foraminifera were carried out at the Center for Marine Environmental Sciences (MARUM), University of Bremen (Bremen, Germany) using a Finnigan MAT 251 isotope ratio mass spectrometer (IRMS) equipped with an automated carbonate preparation device type Kiel I. The standard deviation of the in-house standard was 0.03‰. Analyses of planktonic foraminifera $\delta^{18}O$ were performed at the Paleoceanography and Paleoclimatology Laboratory (P2L), University of São Paulo (São Paulo, Brazil) using a Thermo Scientific MAT 253 IRMS coupled to a Thermo Scientific Kiel IV automated carbonate preparation device. The standard deviation of the in-house standard SHP2L (Crivellari et al., 2021) was 0.08 and 0.07‰ for *G. ruber* and *G. truncatulinoides*, respectively. Measurements are reported in parts per thousand relative to the Vienna Pee Dee Belemnite (VPDB) and have been normalized against repeated measurement of NBS19 standard. NBS19 standard deviation over the measurement period was 0.07 and 0.06‰ for *G. ruber* and *G. truncatulinoides*, respectively.

$\Delta\delta^{18}O$ resulted from calculating *G. truncatulinoides* $\delta^{18}O$ minus *G. ruber* $\delta^{18}O$ from the same sample (depth). Changes in $\delta^{18}O$ recorded by one or both foraminifera species result from temperature or salinity variations of the surrounding seawater, which ultimately can affect the $\Delta\delta^{18}O$. Since temperature and salinity control the density of seawater, high (low) $\Delta\delta^{18}O$ values indicate increased (reduced) upper ocean stratification between the mixed layer and the main thermocline. To remove any linear trend from the $\Delta\delta^{18}O$ record, we used the detrending function of the software MATLAB.

3.4. Mg/Ca analyses from the core GL-1180

For Mg/Ca analyses, between 8 and 20 shells of *G. truncatulinoides* (dextral, 300-425 µm) were handpicked. The cleaning protocol of the *G. truncatulinoides* shells for Mg/Ca analyses followed Barker et al. (2003). Each sample was cleaned with water, methanol, and a hot hydrogen peroxide solution; with no reductive cleaning step. After cleaning, samples were dissolved in dilute HNO_3. Mg/Ca analyses of *G. truncatulinoides* were performed at the MARUM using an inductively coupled plasma optical emission spectrometer (ICP-OES) (Agilent Technologies, 700 Series) with an autosampler (ASX-520 Cetac). Fe, Mn, and Al were measured in addition to Ca and Mg. Three replicates of each sample were measured, and their average was used. The calibration series consisted of one blank and five multi-element standards containing between 20 and 80 ppm of Ca prepared from a mixed standard purchased from SCP Science, France (Mg/Ca of 4.17 mmol/mol). All samples were within the calibrated concentration range. An in-house standard ($Mg/Ca = 2.96$ mmol mol^{-1}), as well as the standards ECRM 752-1 (Bureau of Analysed Standards, Great Britain) and Reinstoff Nr. 3 (Bundesanstalt für Materialforschung und -Prüfung, Germany), were used to verify the accuracy of the measurements and to allow inter-laboratory comparison. The in-house standard was measured every 5 samples, while the other standards were measured every ~90 samples. The standard deviations of the in-house standard, ERCM 752-1 and Reinstoff Nr. 3 were 0.02 mmol mol^{-1} (0.54%, n = 113), 0.02 mmol mol^{-1} (0.47%, n = 8), and 0.01 mmol mol^{-1} (0.70%, n = 8), respectively. Samples with Al/Ca ratio higher than 0.2 mmol mol^{-1} or having Mg/Ca values outside of 4σ of the mean ($\sigma = 0.20$ mmol mol^{-1}) were discarded (four out of 406). The average Al/Ca ratio was 0.02 mmol mol^{-1}. There was no correlation between Mg/Ca and Al/Ca ($R^2 = 0.03$), Mn/Ca ($R^2 = 0.13$), and Fe/Ca ($R^2 = 0.001$).

Temperature was calculated based on the species-specific equation for *G. truncatulinoides* by Regenberg et al. (2009) (r = 0.59) with an accuracy estimation of ±2°C. This equation was chosen due to the following reasons: (1) it was established based on tropical Atlantic top-cores; (2) the size of foraminifera shells used by the authors has a similar range to the shells analyzed here; (3) the same cleaning protocol was used, also without a reductive step.

3.5. Calculation of seawater and foraminifera $\delta^{18}O$ corrected by changes in ice-volume

To calculate the ice-volume-corrected seawater $\delta^{18}O$($\delta^{18}O_{sw\text{-}ivc}$), we used the isotopic paleotemperature equation of Shackleton (1974) following Regenberg et al. (2009). For practical comparison between Vienna Standard Mean Ocean Water (VSMOW) and VPDB we apply an offset of 0.27‰ (Hut, 1987). The temperature component was removed using the Mg/Ca-derived temperatures. The ice-volume effect was removed using the sea level stack of Spratt and Lisiecki (2016), which chronology is based on the LR04 global $\delta^{18}O$ stack (Lisiecki and Raymo, 2005). The ±2°C uncertainty of Mg/Ca-based temperatures (Regenberg et al., 2009) is equivalent

to a change of ~0.5‰ in $\delta^{18}O$. The standard deviation for *G. truncatulinoides* $\delta^{18}O$ measurements is ±0.07‰, and the propagated cumulative root-mean-square error calculated for the $\delta^{18}O_{sw\text{-}ivc}$ is ±0.5‰ (in other words, the analytical error for foraminiferal $\delta^{18}O$ determinations is negligible here).

We used the same sea level stack (Spratt and Lisiecki, 2016) to remove the ice-volume effect from *G. ruber* and *G. truncatulinoides* $\delta^{18}O$ records ($\delta^{18}O_{ivc}$). We used $\delta^{18}O_{ivc}$ of planktonic foraminifera in order to perform spectral analysis of $\delta^{18}O$ records without high latitude orbital components related to ice-volume changes.

3.6. Spectral analysis

REDFIT analyses (Schulz and Mudelsee, 2002) were performed using the software PAST (Hammer et al., 2001) in order to determine the statistically significant periodicities present in our records. We performed the analysis using four segments tapered with a Hanning spectral window. Tests with different numbers of segments did not change the significance of the main frequencies, suggesting that they are a robust feature of our records. To avoid excessive interpolation, we did not perform spectral analysis on Mg/Ca-based thermocline temperature since this record presents some gaps over the last 300 ka.

3.7. Atmospheric modeling

To study the effect of precession on tropical winds over the Atlantic, we performed two experiments using the general circulation model CESM1.2. The state-of-the-art atmosphere model component CAM5 runs with 1.9° × 2.5° horizontal resolution (finite volume core) and with 30 vertical levels. Standard pre-industrial boundary conditions were used except for the orbital parameters, which have been set to Quaternary mean values for eccentricity (0.03) and obliquity (23.4°). In the two experiments, precession was set to its extreme values (90° and 270° longitude of perihelion relative to the moving vernal equinox minus 180°), which reflect maximum (aphelion at boreal summer solstice, i.e., minimum boreal summer insolation) and minimum (perihelion at boreal summer solstice, i.e., maximum boreal summer insolation) precession, respectively. Both experiments, named P_min (minimum precession) and P_max (maximum precession), run for 250 years. Annual means were calculated from the last 50 years of each experiment. Both experiments were initialized with observational ocean data (Steele et al., 2001). Because of the short integration time (due to limited computational resources), the simulations provide no meaningful information about subsurface ocean conditions or deep-ocean circulation changes. We therefore point out that our model experiments are only focusing on changes in atmosphere dynamics under two extreme precessional configurations.

4. Results

4.1. Geochemical proxies

Our planktonic $\delta^{18}O$ records span the last three glacial-interglacial cycles (300 ka). The *G. ruber* $\delta^{18}O$ values vary between −1.70 and 0.67‰ and shows a clear glacial-interglacial pattern. In contrast, the *G. truncatulinoides* $\delta^{18}O$ record, which varies between 0.34 and 2.40‰ (Fig. 2), presents more pronounced variability, particularly during MIS7 and MIS5. The apparent calcification depth (ACD) of the chosen foraminifera species is ~80 m water depth for *G. ruber* and ~250 m water depth for *G. truncatulinoides* (see Text S1 and Fig. S2). A total of 468 paired $\delta^{18}O_{G.\ truncatulinoides}$-$\delta^{18}O_{G.\ ruber}$ ($\Delta\delta^{18}O$) values cover the last ~300 ka at a millennial-scale resolution (Fig. 2b). $\Delta\delta^{18}O$ varies between 0.80 and 3.70‰. Most of our $\Delta\delta^{18}O$ record parallels precession (Fig. 2b).

Here we provide, an almost continuous, Mg/Ca-based temperature record of the WTA main thermocline spanning the last 300 ka. The *G. truncatulinoides* Mg/Ca record from sediment core GL-1180 varies between 1.59 to 2.85 mmol/mol. The mean Mg/Ca-based thermocline temperature is 9.4°C ranging between 3.4 and 15.4°C (Fig. 2c). In the core-top sample, the Mg/Ca-based temperature is 12.6°C, similar to modern temperature at 250 m water depth (11.6°C, Locarnini et al., 2013), which is the calculated ACD of *G. truncatulinoides*. The $\delta^{18}O_{sw\text{-}ivc}$ record (Fig. 2d) vary from −2.05 to 1.42‰ and is strongly coupled with the temperature variations. Thermocline temperatures and $\Delta\delta^{18}O$ are inversely related, with increased thermocline temperatures corresponding to decreased $\Delta\delta^{18}O$ values and thus reduced upper ocean stratification (Fig. 2c).

4.2. Time-series analyses

The frequency spectra of *G. truncatulinoides* $\delta^{18}O$ corrected for changes in ice-volume ($\delta^{18}O_{ivc}$) shows a dominance of precession forcing (~23 ka) (Fig. 3a), while *G. ruber* $\delta^{18}O_{ivc}$ is dominated by 100 ka periodicity (~88 ka) (Fig. 3b). The frequency spectrum of $\Delta\delta^{18}O$ shows a robust signal at the precessional band, with a pronounced peak at 22 ka (Fig. 3c). Secondary peaks in the $\Delta\delta^{18}O$ frequency spectrum (at 95% level) are close to the obliquity and eccentricity bands. Moreover, a peak at 12-13 ka can be observed in the *G. truncatulinoides* $\delta^{18}O_{ivc}$ and $\Delta\delta^{18}O$ records. REDFIT analyses in non-ice-volume-corrected $\delta^{18}O$ records of both foraminifera species indicate the dominance of 100 ka periodicity (Fig. S3).

4.3. Climate model outputs

When forced by maximum and minimum precession, our CESM 1.2 experiments show differences in the annual-average trade winds pattern, ITCZ position, and wind stress curl over the tropical Atlantic when forced by maximum and minimum precession. The climate model results show anomalously strong annual-mean SE trade winds over the tropical Atlantic in experiment P_min relative to P_max (Fig. 4a), while the annual-mean northeastern trade winds were weakened. This agrees with the annual-average northward shift of the ITCZ system and strengthening of the West African monsoon in experiment P_min relative to P_max (Fig. 4b). As a result of the northward shift of the ITCZ system under minimum precession, a large-scale negative wind stress curl anomaly develops in the tropical Atlantic from approximately 10°N to 15°S (Fig. 4a). In the Southern Hemisphere, negative wind stress curl is linked to the divergence of waters at the Ekman layer, resulting in a region of Ekman suction (cyclonic circulation). Therefore, anomalous negative wind stress curl would mean a weakened Ekman pumping or enhanced suction. The latter is mostly the case for the equatorial and tropical South Atlantic since this region is already dominated by a cyclonic circulation. In the South Atlantic, an anomalous positive wind stress curl forces an enhanced anticyclonic circulation to the south of 15°S. The annual averaged zero wind stress curl line at the limit between the tropical cyclonic and subtropical anticyclonic circulation in the South Atlantic is displaced southward during minimum precession due to the expansion of the cyclonic circulation in the tropical Atlantic.

5. Discussion

5.1. Precessional signal in the western tropical Atlantic

Following previous studies (Venancio et al., 2018; Mulitza et al., 1997), high (low) values of $\Delta\delta^{18}O$ calculated between deep-

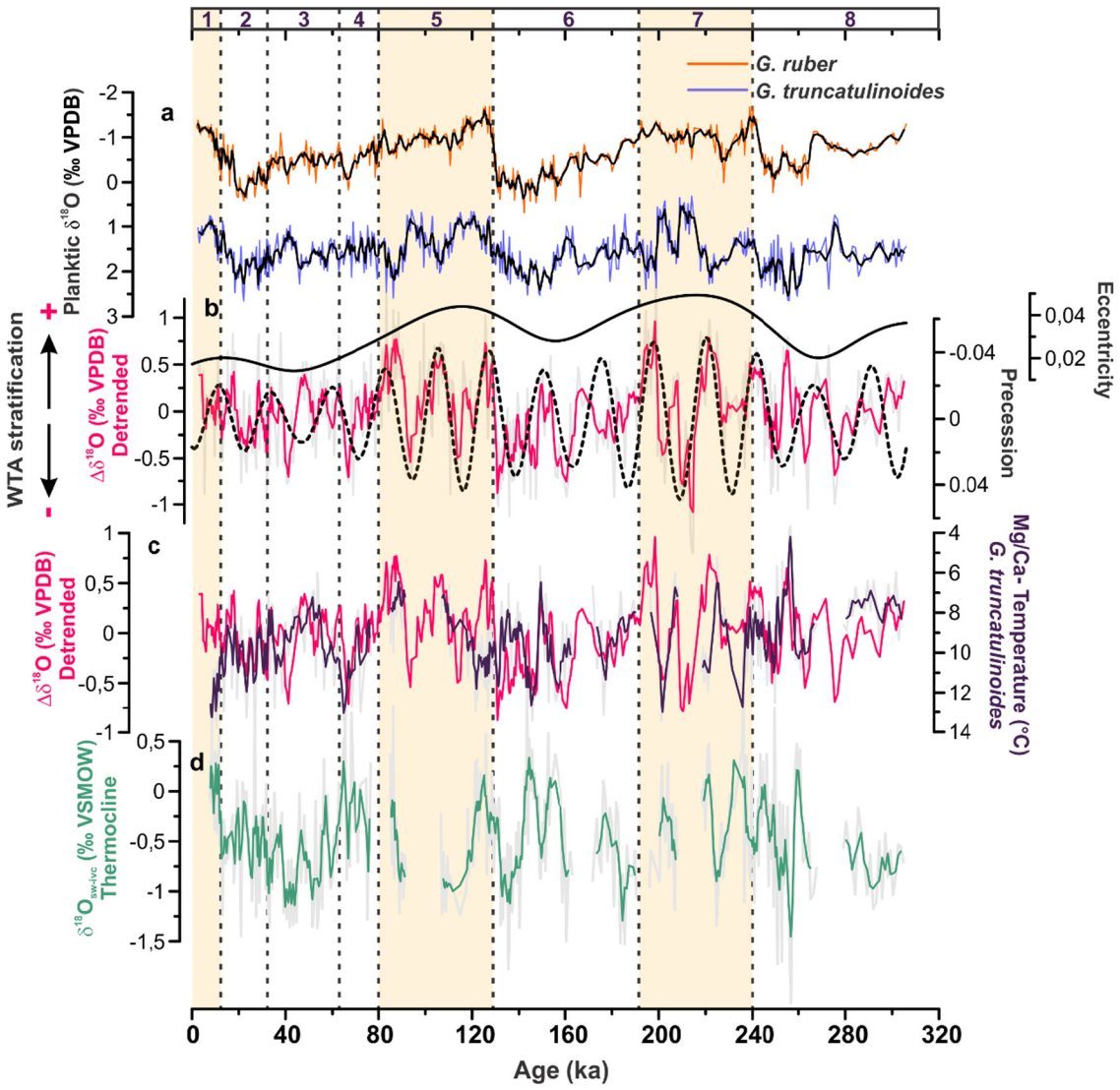

Fig. 2. Stable oxygen isotopes ($\delta^{18}O$), Mg/Ca-based temperatures and derived data ($\Delta\delta^{18}O$ and $\delta^{18}O$ of seawater) from sediment core GL-1180 together with orbital parameters. a) $\delta^{18}O$ of *Globigerinoides ruber* (orange) and *Globorotalia truncatulinoides* (dark blue) with 3-points running averages (black); b) linearly detrended $\Delta\delta^{18}O$ ($\delta^{18}O_{G.\ truncatulinoides}$ - $\delta^{18}O_{G.\ ruber}$) (light grey line) with 3-points running average (pink); the black continuous line represents eccentricity and the black dashed line shows precession; c) Mg/Ca-based temperatures obtained from *G. truncatulinoides* (light grey line) with 3-points running average (purple) and 3-points running average of linearly detrended $\Delta\delta^{18}O$ (light pink); note that the temperature axis is inverted; d) main thermocline ice-volume-corrected $\delta^{18}O$ of seawater ($\delta^{18}O_{sw\text{-}ivc}$) as a proxy for relative changes in main thermocline salinity (light grey line) with 3-points running average (green). Values were reconstructed from the $\delta^{18}O$ and Mg/Ca-based temperature of *G. truncatulinoides*. Numbers at the top x-axis indicate Marine Isotope Stages (MIS), while colored bars denote interglacial periods.

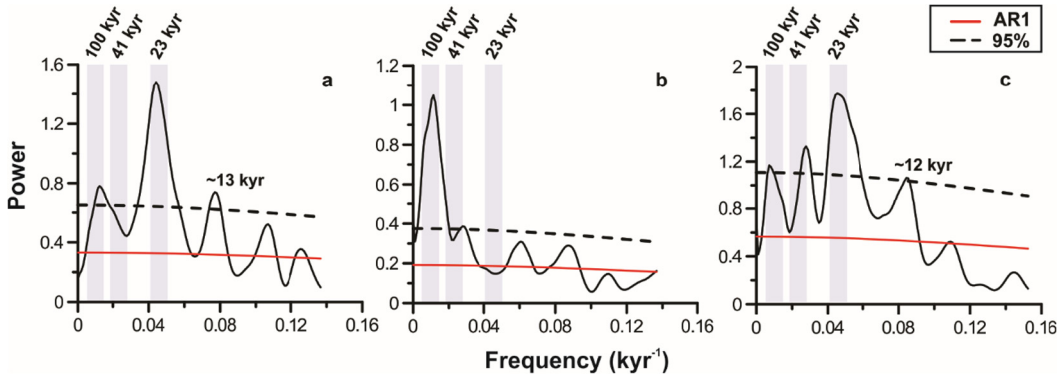

Fig. 3. Time-series analyses performed on planktonic $\delta^{18}O$ corrected for changes in ice-volume ($\delta^{18}O_{ivc}$) (see section 3.6) and $\Delta\delta^{18}O$ from sediment core GL-1180. a) *Globorotalia truncatulinoides* $\delta^{18}O_{ivc}$; b) *Globigerinoides ruber* $\delta^{18}O_{ivc}$; c) $\Delta\delta^{18}O$ calculated as $\delta^{18}O_{G.\ truncatulinoides}$ - $\delta^{18}O_{G.\ ruber}$. The red line (AR1) represents the red noise spectrum, and the dashed line represents the false alarm level at 95%. The REDFIT algorithm (Schulz and Mudelsee, 2002) was used to perform the analyses. The light grey bars highlight the bands of eccentricity, obliquity, and precession.

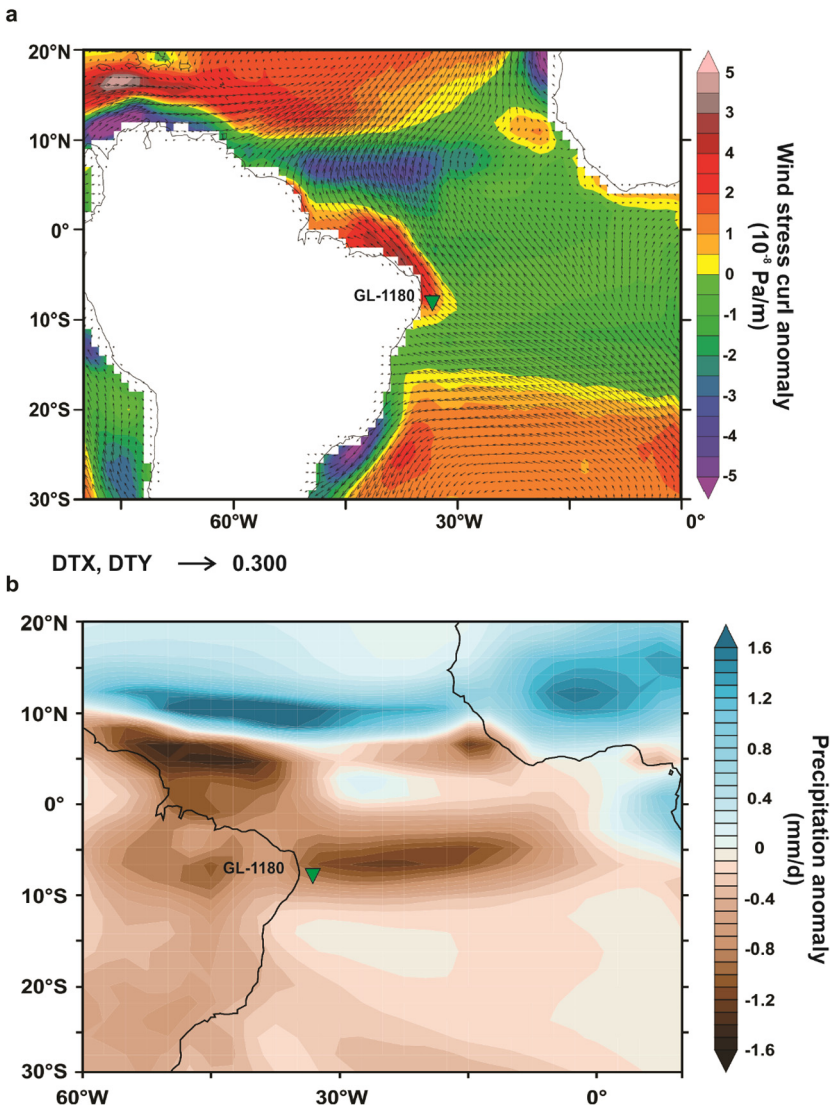

Fig. 4. Effect of precession on annual mean anomaly (experiment P_min minus P_max) of wind stress and precipitation as simulated by CESM1.2. a) Wind stress anomaly. Arrows indicate the modeled wind stress (Pa) anomaly. Colors show the difference in wind stress curl (in units of 10^{-8} Pa/m). In the Southern Hemisphere, negative values (cool colors) indicate anomalous cyclonic circulation (divergence), while positive values (warm colors) indicate anomalous anticyclonic circulation (convergence). b) Precipitation anomaly. Colors show the precipitation anomaly (in units of mm/d). Positive (negative) values indicate anomalous increase (decrease) in precipitation.

and shallow-dwelling foraminiferal $\delta^{18}O$ are interpreted as increased (reduced) upper ocean stratification (Fig. 2b). In general, increased (reduced) WTA stratification fits remarkably with minimum (maximum) precession (Figs. 2b, 3c). This strongly suggests that precession forcing modulated the WTA upper ocean stratification over the late Pleistocene. The amplitude of $\Delta\delta^{18}O$ variations is noticeably increased during periods of high eccentricity (Fig. 2b), highlighting the modulating effect of eccentricity on the amplitude of precession changes, and hence on the amplitude of our $\Delta\delta^{18}O$ record. The influence of obliquity on stratification is also indicated by our $\Delta\delta^{18}O$ frequency spectrum (Fig. 3c). This could be caused by obliquity-forced variations in the meridional temperature gradient, affecting the Southern Hemisphere westerlies (Mantsis et al., 2014; Timmermann et al., 2014; Mantsis et al., 2011) and the Ekman pumping at midlatitudes, eventually transporting the obliquity signal towards the tropical Atlantic via SACW. However, no evidence of an obliquity signal is observed in the frequency spectrum of *G. truncatulinoides* $\delta^{18}O_{ivc}$ (Fig. 3). Alternatively, obliquity-forced fluctuations in the meridional temperature gradient could affect the intensity of the southeastern trade winds, causing variations in the WTA mixed layer temperature due to changes in wind stress (Hou et al., 2020). This mechanism potentially imprinted the obliquity signal in the WTA ocean surface.

We observe a peak centered at 12 and 13 ka in our $\Delta\delta^{18}O$ and *G. truncatulinoides* $\delta^{18}O_{ivc}$ frequency spectra, respectively (Fig. 3a, c). This period is consistent with the half-precession cycle (11.5 ka) found in the intertropical belt (Berger and Loutre, 1997; Berger et al., 2006) and with results from previous paleoceanographic studies in the WTA (Venancio et al., 2018; Niemitz and Billups, 2005). In the intertropical zone, the sun passes overhead twice a year (at the equinoxes). Over a precession cycle, this produces two peaks of insolation maxima and the half-precession component (Rutherford and D'Hondt, 2000; Berger and Loutre, 1997). Although half-precession signal decreases with the distance from the equator, it can be observed in the whole intertropical belt (Berger et al., 2006). Additionally, the half-precession signal can be amplified by a nonlinear response of the climate system to precessional forcing on tropical insolation (Hagelberg et al., 1994). Eventually, this sub-orbital component can be imprinted on the upper ocean hydrography through changes in the atmospheric circulation dynamics. Recently, a half-precession signal was identified in a stratification record from the western tropical Pacific (core MD01-2386), but it

was attributed to the influence of waters sourced from both hemispheres (Jian et al., 2020). Although the mechanism imprinting the half-precession signal to our records is not completely understood, our data imply that this suborbital frequency can be found at the main thermocline in regions where waters are exclusively sourced from the Southern Hemisphere.

The dominance of precession in $\Delta\delta^{18}O$ and *G. truncatulinoides* $\delta^{18}O_{ivc}$ indicates that the dynamics of the main thermocline controls the WTA stratification. The covariation between $\Delta\delta^{18}O$ and Mg/Ca-based main thermocline temperatures corroborates that the WTA upper stratification mostly responds to changes in the thermal structure of the main thermocline (Fig. 2c). High (low) $\Delta\delta^{18}O$ values reflecting high (low) stratification are generally related to low (high) thermocline temperatures. The convergence between these two independent geochemical methods (stable isotopes and Mg/Ca-based temperature) supports that our $\Delta\delta^{18}O$ values indeed record changes in upper ocean stratification, mostly driven by hydrographic changes in the main thermocline. The spectral analysis of *G. ruber* $\delta^{18}O_{ivc}$ record (Fig. 3b) suggests that the WTA surface water density was controlled by glacial-interglacial climate variability.

Between ~140 and ~120 ka thermocline temperature and $\Delta\delta^{18}O$ oscillate in opposition to the scheme described above. During this interval, the long-term variability shows that high thermocline temperature coincides with a high stratification and vice versa (Fig. 5b, c). We suggest that the cold MIS 6 glacial maximum and the warm MIS 5e interglacial changed the thermocline temperature in the opposite way to what is observed throughout most of the $\Delta\delta^{18}O$ record, dampening the temperature variability. In other words, the mechanism governing the WTA stratification through most of the record (see the section below) may have been suppressed by the glacial and interglacial boundary conditions around Termination II. The dampened temperature variability is reflected in the dominance of salinity on *G. truncatulinoides* $\delta^{18}O$. The $\delta^{18}O_{sw\text{-}ivc}$ increases by ~1.2‰ during Termination II (Fig. 5e). This salinity effect was possibly boosted by an increase in South Atlantic thermocline salinity at the beginning of Termination II (Fig. 5e, f) (Ballalai et al., 2019), probably due to increases in the advection of saline waters from the Indian Ocean to the South Atlantic thermocline (Scussolini et al., 2015). A decoupling between $\Delta\delta^{18}O$ and temperature is also noticed during Termination I and the Holocene (Fig. 2c), which could possibly indicate a recurring feature of glacial terminations, though a further investigation would be required.

Using published *G. ruber* and *G. inflata* $\delta^{18}O$ data from sediment core GL-1090 (Santos et al., 2017a, b; Santos et al., 2020) together with new *G. inflata* $\delta^{18}O$ results from the same core, we reconstructed the upper ocean stratification in the subtropical western South Atlantic (24°S) over the last 182 ka (see Text S2 and Fig. S4). The spectral analysis of the $\Delta\delta^{18}O$ record between *G. inflata* and *G. ruber* shows an outstanding dominance of the obliquity component (Fig. S5). This result agrees with the notion that ventilation of the main thermocline in mid-latitudes is forced by the westerlies (Luyten et al., 1983a), which are modulated by obliquity (Timmermann et al., 2014). However, as indicated by the frequency spectrum of *G. truncatulinoides* $\delta 18O_{ivc}$, it is unlikely that this obliquity signal has propagated to the WTA thermocline. The frequency data strongly supports that changes in WTA stratification are primarily controlled by a precession-paced tropical mechanism while the subtropical southwestern Atlantic is controlled by obliquity-driven mid-latitudes variability.

A $\Delta\delta^{18}O$ record from core GL-1248 calculated with $\delta^{18}O$ from *G. ruber* (white) and *Neogloboquadrina dutertrei* (Fig. S6), a species recording the seasonal thermocline, identified a precessional modulation in the stratification over the last 130 ka in the western equatorial Atlantic (see location in Fig. 1; Venancio et al., 2018). In

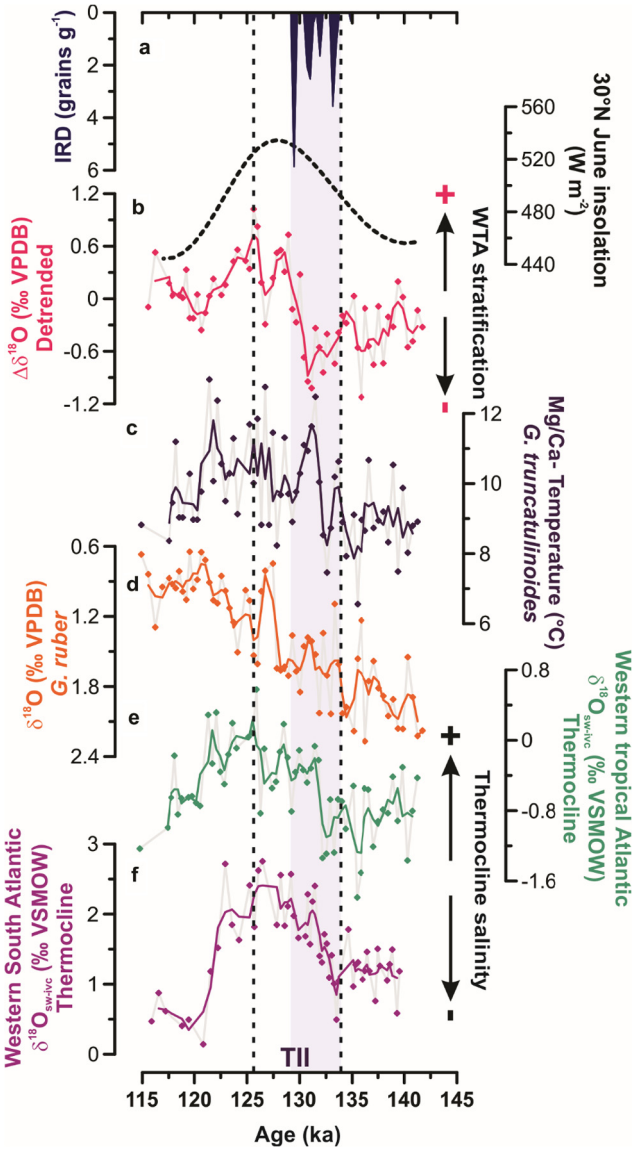

Fig. 5. WTA upper ocean stratification and thermocline temperature around Termination II (TII). a) Ice-rafted debris (IRD) from ODP Site 1063 (Deaney et al., 2017); b) 3-points running average of linearly detrended $\Delta\delta^{18}O$ (pink) and June isolation at 30° N (dotted line) (Laskar et al., 2004); c) Mg/Ca-based temperature of *G. truncatulinoides* (dark purple) from GL-1180; d) $\delta^{18}O$ of *G. truncatulinoides* (orange) with 5-points running average; e) thermocline ice-volume-corrected seawater $\delta^{18}O$ ($\delta^{18}O_{sw\text{-}ivc}$) as a proxy for relative changes in thermocline salinity (green); f) $\delta^{18}O_{sw\text{-}ivc}$ from site GL-1090 (Ballalai et al., 2019) (light purple). The light grey bar marks Heinrich stadial 11. Data are presented in the original age model of the quoted studies.

line with the present study, the authors reasoned that strong stratification in that region was related to minimum precession. This shows that the WTA seasonal and main thermocline varied on the same orbital pace, but driven by distinct mechanisms, as discussed below.

5.2. Climate mechanism driving stratification changes in the WTA

Our $\Delta\delta^{18}O$ record shows a remarkable fit with boreal summer low latitude insolation (Fig. 6a), which is dominated by precession (Clement et al., 2004; Berger and Loutre, 1997; Berger et al., 1993). High $\Delta\delta^{18}O$ (enhanced stratification) in the WTA consistently occurs when boreal summer is close to perihelion. In fact, our $\Delta\delta^{18}O$ record reveals a coupling with the ^{230}Th-normalized Sahara dust flux, which is controlled by the precession-driven

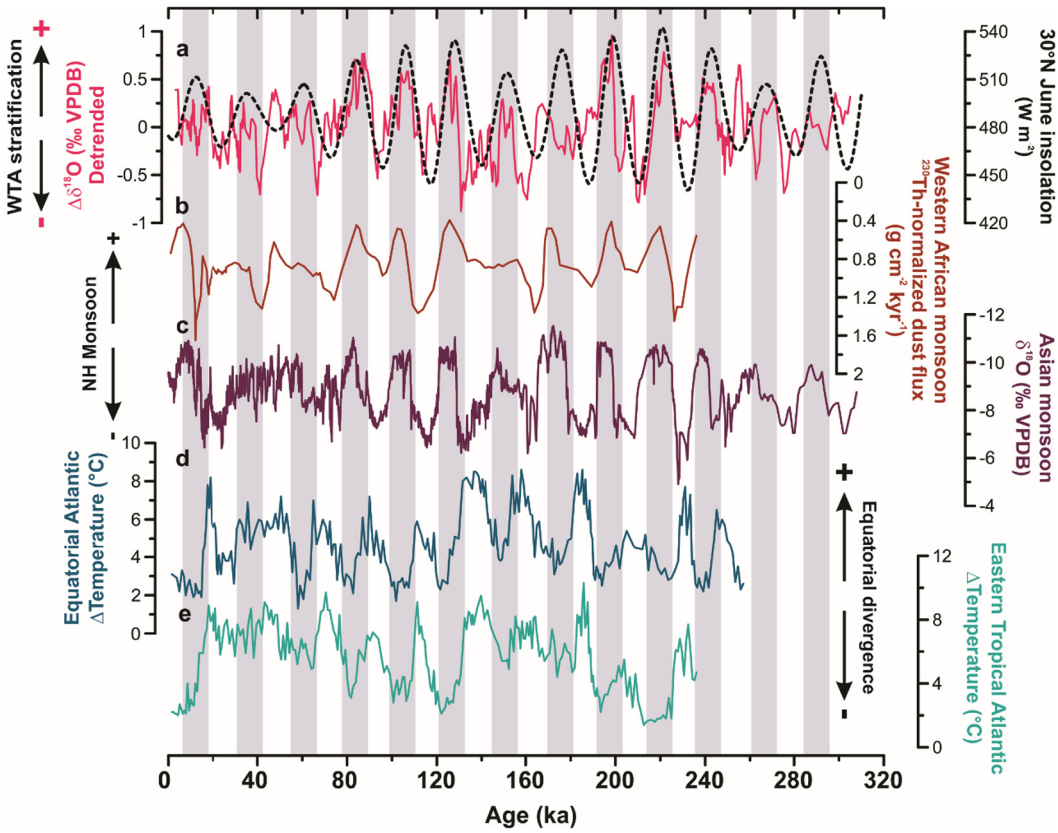

Fig. 6. Comparison between $\Delta\delta^{18}O$ from GL-1180 with processional-modulated records associated with North Hemisphere monsoon systems and Tropical Atlantic divergence zone. a) 3-points running average of linearly detrended $\Delta\delta^{18}O$ (pink) from core GL-1180. The dashed line represents June insolation at 30° N (Laskar et al., 2004); b) ^{230}Th-normalized Sahara dust fluxes from sediment core MD03-2705 (brown; 3-points running average) (Skonieczny et al., 2019); c) speleothem $\delta^{18}O$ record of Asian monsoon system (dark purple) (Cheng et al., 2016); d) Equatorial Atlantic seasonal Δtemperature record (summer temperature - winter temperature) based on transfer function (site V30-40) (blue) and e) same as d in the eastern tropical Atlantic (ETA) (site RC24-16) (cyan) (Mcintyre et al., 1989). High ΔT indicates strong ETA divergence. Grey bars are aligned with high boreal summer insolation at 30°N. All data are presented in the original age model of the quoted studies.

Western African Monsoon (Skonieczny et al., 2019; Fig. 6b) and with $\delta^{18}O$ of speleothems from China recording the Asian monsoon system (Cheng et al., 2016; Fig. 6c). In both cases, enhanced WTA stratification coincided with intense Northern Hemisphere monsoons. Our record is also coupled with equatorial Atlantic and eastern tropical Atlantic (ETA) divergence/stratification (Mcintyre et al., 1989; Fig. 6d, e), which is controlled by WAM-driven SE trade winds zonality (Mcintyre and Molfino, 1996; Molfino and Mcintyre, 1990; Mcintyre et al., 1989). Plausible mechanisms connecting Northern Hemisphere monsoon systems, ETA divergence and WTA upper-ocean stratification should comprise processes linked to the ITCZ system.

So far, the precession-modulated seasonal thermocline stratification in the tropical Atlantic has been ascribed to the influence of WAM-modulated SE trade winds (Venancio et al., 2018; Mcintyre and Molfino, 1996). According to this explanation, the increase (decrease) in SE trade winds zonality due to a weak (strong) WAM boosts (hinders) the westward South Equatorial Current piling up warm waters in the WTA, increasing the temperature of the seasonal thermocline and weakening the stratification. This interpretation is in line with our $\Delta\delta^{18}O$ record, which shows decreased WTA stratification during precession maxima (Fig. 6). However, this explanation applies to the shallow seasonal thermocline. At site GL-1180, *G. truncatulinoides* ACD is approximately 250 m water depth, recording the main thermocline. At this depth, seasonal temperature variations are negligible (Locarnini et al., 2013). Therefore, the precession-modulated piling up of warm waters in the WTA, as previously suggested (Venancio et al., 2018), is insufficient to explain our reconstructed changes, of 4-5°C, in the main thermocline temperature (Fig. 2c). Additionally, our annual average CESM1.2 experiments do not show reduced zonality of the SE trade winds due to enhanced WAM during precession minima (Fig. 4a), although it must be more evident during the boreal summer.

We suggest an alternative ocean-atmosphere mechanism that connects the dynamics of the SE trade winds to the SASG. The SASG is marked by a deep mixed layer filled with warm and saline waters, the northern extension of which is limited by the position of the sSEC (Marcello et al., 2018; Rodrigues et al., 2007; Stramma, 1991). Towards the equator, the thermocline becomes shallower due to the equatorial divergence that brings up colder and fresher waters to the subsurface. At present, the sSEC bifurcates near the Brazilian continental margin between 10-14°S (Rodrigues et al., 2007). During the annual cycle, the sSEC bifurcation migrates latitudinally, driven by Sverdrup dynamics related to the position of the ITCZ and associated changes in the wind stress curl over the ocean (Rodrigues et al., 2007). During boreal spring/summer (autumn/winter), the ITCZ migrates northwards (southwards) expanding the negative (positive) wind stress curl and an anomalous cyclonic (anticyclonic) circulation in the western tropical South Atlantic, shoaling (deepening) the thermocline north of the sSEC bifurcation, while pushing the zero wind stress curl line and the sSEC bifurcation southwards (northwards) (Rodrigues et al., 2007).

This seasonal mechanism can be applied to the orbital-scale. In the minimum precession case (boreal summer insolation maximum), the ITCZ shifts northward and consequently a large-scale anomaly of negative wind stress curl associated with an anomalous cyclonic circulation develops in the tropical South Atlantic as simulated in our CESM1.2 experiments (Fig. 4a and b). This cyclonic circulation leads to enhanced Ekman suction in the tropics,

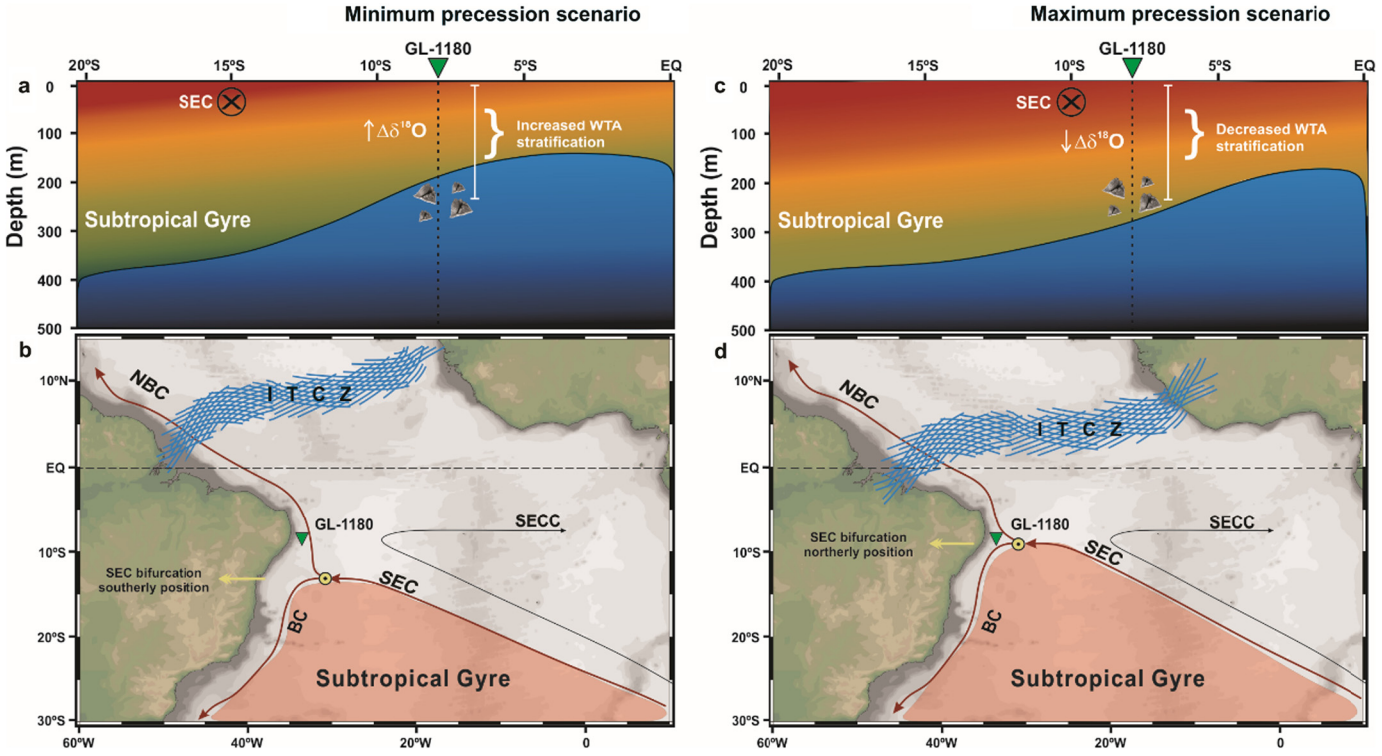

Fig. 7. Schematic representation of the South Equatorial Current (SEC), South Atlantic Subtropical Gyre (SASG) and Intertropical Convergence Zone (ITCZ) latitudinal displacement, together with changes in thermocline stratification during minimum (left panels) and maximum (right panels) precession scenarios. Upper panels) Schematic zonal sections of the tropical South Atlantic illustrating the vertical displacement of the main thermocline and intrusion of SASG waters towards the equator during a) minimum precession (boreal summer at perihelion) and c) maximum precession (boreal summer at aphelion). Lower panels) Schematic map of the latitudinal displacement of the SEC and the SASG relative to the position of sediment core GL-1180 during b) minimum precession and d) maximum precession. Warm and cool colors in the upper panels indicate warm and cold waters, respectively. Background colors are illustrative. BC: Brazil Current, NBC: North Brazil Current, SECC: South Equatorial Counter Current.

shoaling the main thermocline and forcing the southward displacement of the sSEC bifurcation and hence of the SASG northern edge (Fig. 7). Considering that core GL-1180 is located at ~8°S, this site is sensitive to variations in the latitude of the sSEC bifurcation (Fig. 1). Therefore, during periods of boreal summer insolation maximum (precession minima), the warm subsurface waters of the SASG move southward of the latitude of core GL-1180 as the thermocline shoals, eventually increasing upper ocean stratification north of the sSEC bifurcation (Fig. 7). The opposite situation occurs during periods of precession maxima. As an example, the temperature difference at 250 m water depth between two temperature profiles (Locarnini et al., 2013), slightly to the north (6.5°S) and south (12.5°S) of GL-1180, is 3.6°C (Fig. S7). This supports our argument that shifting the northernmost SASG limit would significantly affect the main thermocline temperature at the site of GL-1180.

The mechanism presented here does not invalidate the role of WAM-modulated trade winds zonality in piling up waters in the WTA. However, we argue that this mechanism alone is insufficient to explain significant temperature changes at ~250 m water depth, as presented in our study.

5.3. Does precession-driven WTA stratification have implications for cross-equatorial transport and AMOC strength?

Since the WTA circulation is part of the upper limb of the AMOC (Zhang et al., 2011; Yang, 1999), our data and the proposed mechanism for changes in upper WTA stratification may have implications for orbital-scale cross-equatorial heat and salt transport in the Atlantic.

Studies show that the rate of deep-water formation in the North Atlantic is out of phase with precession minima (Lisiecki, 2014; Lisiecki et al., 2008), that is, the AMOC seems to be weaker during boreal summer insolation maxima. However, the mechanism whereby AMOC responds to precession is still not clear (Toggweiler and Lea, 2010; Lisiecki et al., 2008). Here, we propose that periods of high WTA stratification (precession minima) could be related to a decrease in the northward transport of warm and salty upper ocean waters. Ultimately, this would result in the propagation of precessional-modulated tropical variability to the high latitude North Atlantic.

According to our proposed mechanism (section 5.2), during periods of high WTA stratification, warm and saline subsurface waters of the SASG are prevented from advancing towards the equator. This is supported by the low temperature and low $\delta^{18}O_{sw\text{-}ivc}$ values of the thermocline observed during periods of high WTA stratification (Fig. 2). Consequently, during precession minima, the poor penetration of warm and saline SASG waters in the WTA can reduce the cross-equatorial flow towards the North Atlantic. In contrast, during precession maxima, the northward SASG expansion and the deeper WTA thermocline allows for the penetration of warm and saline subsurface waters towards the equator, increasing the cross-equatorial transport. This idea is in line with a mid-Pleistocene record of *G. truncatulinoides* (sinistral) abundance from the western tropical North Atlantic, which indicates increased (reduced) interhemispheric water transport during precession maxima (minima) (Kaiser et al., 2019). Besides, this hypothesis agrees with the strong AMOC observed during periods of maximum precession (Lisiecki et al., 2008). Although this link between tropical and high latitudes of the North Atlantic is only theoretical, our findings reopen the discussion about the sensitivity of the AMOC not only to boreal high latitude summer insolation (Imbrie et al., 1992) but also to tropical forcing (Mcintyre and Molfino, 1996).

6. Conclusions

δ^{18}O and Mg/Ca records of planktonic foraminifera species from core GL-1180 collected in the WTA show robust evidence of precessionally modulated upper ocean stratification changes in the WTA over the last 300 ka. The precessional pace is more strongly expressed in the main thermocline rather than the surface ocean. We propose a new mechanism that explains changes in upper WTA stratification by changes in low latitude insolation. During periods of high boreal summer insolation (precession minimum), the development of an anomalous cyclonic circulation over the tropical South Atlantic due to the northward shift of the ITCZ shoals the thermocline at the equator and forces the southward migration of the SASG northern boundary. This situation shoals the main thermocline of the WTA while prevents the transport of warm and saline subsurface waters of the SASG towards the equatorial Atlantic, increasing the WTA upper ocean stratification. Finally, we hypothesize that strong WTA stratification during precession minima reduces the cross-equatorial transport of heat and salt, which may weaken the AMOC, although this connection would require further investigation.

CRediT authorship contribution statement

Nascimento, R.A.: Writing – original draft, Formal analysis, Conceptualization. **Venancio, I.M., Chiessi, C.M., Ballalai, J.M., Kuhnert, H., Johnstone, H., Santos, T.P., Govin, A., and Mulitza, S.:** Writing – review & editing. **Prange, M.:** Numeric modeling, Writing – review & editing. **Crivellari, S.:** Formal analysis, review & editing. **Albuquerque, A.L.S.:** Supervision, Project administration, Funding acquisition

Declaration of competing interest

The authors declare that they have no known competing financial interests or personal relationships that could have appeared to influence the work reported in this paper.

Acknowledgements

We thank the Petrobras for providing the sediment core used in this study. This study was supported by the CAPES-ASpECTO project (grant 88887.091731/2014-01) CNPq-Aspecto (grant 429767/2018-8), CAPES-PRINT CLIMATE Project (grant 88887.310301/2018-00) and CNPq Project RAiN (grant 406322/2018-0). R.A. Nascimento acknowledges the scholarship from CAPES (grant 88887.176103/2018-00). CAPES also financially supported I.M.V. with a scholarship (grant 88887.156152/2017-00). C.M.C. acknowledges the financial support from FAPESP (grants 2018/15123-4 and 2019/24349-9), CAPES (grants 564/2015 and 88881.313535/2019-01), CNPq (grant 312458/2020-7), and the Alexander von Humboldt Foundation. ALSA is a senior scholar CNPq (grant 302521/2017-8). We also acknowledge the partial support from the Coordenação de Aperfeiçoamento de Pessoal de Nível Superior – Brasil (CAPES) – Finance Code 001. This is LSCE publication number 7665. All data presented in this manuscript are available at https://doi.org/10.1594/PANGAEA.921841.

Appendix A. Supplementary material

Supplementary material related to this article can be found online at https://doi.org/10.1016/j.epsl.2021.117030.

References

Ballalai, J.M., Santos, T.P., Lessa, D.O., Venancio, I.M., Chiessi, C.M., Johnstone, H.J.H., Kuhnert, H., Claudio, M.R., Toledo, F., Costa, K.B., Albuquerque, A.L.S., 2019. Tracking spread of the Agulhas leakage into the western South Atlantic and its northward transmission during the last interglacial. Paleoceanogr. Paleoclimatol. 34 (11), 1744–1760. https://doi.org/10.1029/2019PA003653.

Barker, S., Greaves, M., Elderfield, H., 2003. A study of cleaning procedures used for foraminiferal Mg/Ca paleothermometry. Geochem. Geophys. Geosyst. 4 (9), 1–20. https://doi.org/10.1029/2003GC000559.

Berger, A.L., Loutre, M.F., Mélice, J.L., 2006. Equatorial insolation: from precession harmonics to eccentricity frequencies. Clim. Past 2 (4), 519–533. https://doi.org/10.5194/cpd-2-519-2006.

Berger, A., Loutre, M.F., 1997. Intertropical latitudes and half-precessional cycles. Science 278, 1476–1478. https://doi.org/10.1126/science.278.5342.1476.

Berger, A., Loutre, M.F., Tricot, C., 1993. Insolation and Earth's orbital periods. J. Geophys. Res. 98 (D6). https://doi.org/10.1029/93jd00222.

Birch, H., Coxall, H.K., Pearson, P.N., Kroon, D., O'Regan, M., 2013. Planktonic foraminifera stable isotopes and water column structure: disentangling ecological signals. Mar. Micropaleontol. 101, 127–145. https://doi.org/10.1016/j.marmicro.2013.02.002.

Blaauw, M., Christen, J.A., 2011. Flexible paleoclimate age-depth models using an autoregressive gamma process. Bayesian Anal. 6 (3), 457–474. https://doi.org/10.1214/11-BA618.

Cheng, H., Lawrence Edwards, R., Sinha, A., Spötl, C., Yi, L., Chen, S., Zhang, H., 2016. The Asian monsoon over the past 640,000 years and ice age terminations. Nature 534 (7609), 640–646. https://doi.org/10.1038/nature18591.

Clement, A.C., Hall, A., Broccoli, A.J., 2004. The importance of precessional signals in the tropical climate. Clim. Dyn. 22 (4), 327–341. https://doi.org/10.1007/s00382-003-0375-8.

COHMAP Members, 1988. Climatic changes of the last 18,000 years: observations and model simulations. Science 241, 1043–1052.

Crivellari, S., Viana, P.J., Campos, M.C., Kuhnert, H., Barros, A., Cruz, F.W., Chiessi, C.M., 2021. Development and characterization of a new in-house reference material for stable carbon and oxygen isotopes analyses. J. Anal. At. Spectrom. https://doi.org/10.1039/D1JA00030F.

Deaney, E.L., Barker, S., Van de Flierdt, T., 2017. Timing and nature of AMOC recovery across Termination 2 and magnitude of deglacial CO_2 change. Nat. Commun. 8 (1), 1–10. https://doi.org/10.1038/ncomms14595.

Elderfield, H., Vautravers, M., Cooper, M., 2002. The relationship between shell size and Mg/Ca, Sr/Ca, δ 18 O, and δ 13 C of species of planktonic foraminifera. Geochem. Geophys. Geosyst. 3 (8), 1–13. https://doi.org/10.1029/2001gc000194.

Govin, A., Capron, E., Tzedakis, P.C., Verheyden, S., Ghaleb, B., Hillaire-Marcel, C., et al., 2015. Sequence of events from the onset to the demise of the Last Interglacial: Evaluating strengths and limitations of chronologies used in climatic archives. Quat. Sci. Rev. 129, 1–36. https://doi.org/10.1016/j.quascirev.2015.09.018.

Hagelberg, T.K., Bond, G., deMenocal, P., 1994. Milankovitch band forcing of sub-Milankovitch climate variability during the Pleistocene. Paleoceanography 9, 545. https://doi.org/10.1029/94PA00443.

Hammer, Ø., Harper, D.A.T., Ryan, P.D., 2001. PAST: paleontological statistics software package for education and data analysis. Palaeontol. Electronica 76 (4), 1–9. https://doi.org/10.1016/j.bcp.2008.05.025.

Hazeleger, W., Drijfhout, S., 2006. Subtropical cells and meridional overturning circulation pathways in the tropical Atlantic. J. Geophys. Res. 111, C03013. https://doi.org/10.1029/2005JC002942.

Hou, A., Bahr, A., Schmidt, S., Strebl, C., Albuquerque, A.L., Chiessi, C.M., Friedrich, O., 2020. Forcing of western tropical South Atlantic sea surface temperature across three glacial-interglacial cycles. Glob. Planet. Change 188, 103150. https://doi.org/10.1016/j.gloplacha.2020.103150.

Hut, G., 1987. Stable isotope reference samples for geochemical and hydrological investigations. In: Report of Consultant's Group Meeting. International Atomic Energy Agency, Vienna, Austria, p. 42.

Imbrie, J., et al., 1992. On the structure and origin of major glaciation cycles, 1, linear responses to Milankovitch forcing. Paleoceanography 7 (6), 701–738. https://doi.org/10.1029/92PA02253.

Jian, Z., Wang, Y., Dang, H., Lea, D.W., Liu, Z., Jin, H., Yin, Y., 2020. Half-precessional cycle of thermocline temperature in the western equatorial Pacific and its bihemispheric dynamics. Proc. Natl. Acad. Sci. USA 117 (13), 7044–7051. https://doi.org/10.1073/pnas.1915510117.

Kaiser, E.A., Caldwell, A., Billups, K., 2019. North Atlantic upper-ocean hydrography during the mid-Pleistocene transition evidenced by globorotalia truncatulinoides coiling ratios. Paleoceanogr. Paleoclimatol. 34, 658–671. https://doi.org/10.1029/2018PA003502.

Kutzbach, J.E., Guetter, P.J., 1986. The influence of changing orbital parameters and surface boundary conditions on climate simulations for the past 18 000 years. J. Atmos. Sci. 45 (10), 1726–1759.

Kutzbach, J.E., Liu, Z., 1997. Response of the African monsoon to orbital forcing and ocean feedbacks in the middle Holocene. Science 278 (5337), 440–443. https://doi.org/10.1126/science.278.5337.440.

Kutzbach, J.E., Otto-Bliesner, B.L., 1982. The sensitivity of the African- Asian monsoonal climate to orbital parameter changes for 9000 years B.P. in a low-resolution general circulation model. J. Atmos. Sci. https://doi.org/10.1175/1520-0469(1982)039<1177:TSOTAA>2.0.CO;2.

Laskar, J., Robutel, P., Joutel, F., Gastineau, M., Correia, A.C.M., Levrard, B., 2004. A long-term numerical solution for the insolation quantities of the Earth. Astron. Astrophys. 428, 261–285. https://doi.org/10.1051/0004-6361:20041335.

Lisiecki, L.E., Raymo, M.E., 2005. A Pliocene-Pleistocene stack of 57 globally distributed benthic δ 18O records. Paleoceanography 20 (1), 1–17. https://doi.org/10.1029/2004PA001071.

Lisiecki, L.E., Raymo, M.E., Curry, W.B., 2008. Atlantic overturning responses to Late Pleistocene climate forcings. Nature 456 (7218), 85–88. https://doi.org/10.1038/nature07425.

Lisiecki, L.E., 2014. Atlantic overturning responses to obliquity and precession over the last 3 Myr. Paleoceanography 29, 71–86. https://doi.org/10.1002/2013PA002505.

Locarnini, R.A., Mishonov, A.V., Antonov, J.I., Boyer, T.P., Garcia, H.E., Baranova, O.K., et al., 2013. World ocean atlas 2013, volume 1: temperature. In: Levitus, S., Mishonov, A. (Eds.), NOAA Atlas NESDIS 73. U.S. Government Printing Office, Silver Spring, MD, p. 40.

Lumpkin, R., Speer, K., 2003. Large-scale vertical and horizontal circulation in the North Atlantic Ocean. J. Phys. Oceanogr. 33, 1902–1920. https://doi.org/10.1175/1520-0485(2003)033%3C1902:LVAHCI%3E2.0.CO;2.

Luyten, J., Pedlosky, J., Stommel, H., 1993b. Climatic inferences from the ventilated thermocline. Clim. Change 5, 183–191. https://doi.org/10.1007/BF02423489.

Luyten, J.R., Pedlosky, J., Stommel, H., 1983a. The ventilated thermocline. J. Phys. Oceanogr. 13, 292–309. https://doi.org/10.1175/1520-0485(1983)013<0292:TVT>2.0.CO;2.

Mantsis, D.F., Clement, A., Broccoli, A., Erb, M., 2011. Climate feedbacks in response to changes in obliquity. J. Climate 24, 2830–2845. https://doi.org/10.1175/2010JCLI3986.1.

Mantsis, D.F., Lintner, B.R., Broccoli, A.J., Erb, M.P., Clement, A.C., Park, H.S., 2014. The response of large-scale circulation to obliquity-induced changes in meridional heating gradients. J. Climate 27 (14), 5504–5516. https://doi.org/10.1175/JCLI-D-13-00526.1.

Marcello, F., Wainer, I., Rodrigues, R.R., 2018. South Atlantic Subtropical Gyre late twentieth century changes. J. Geophys. Res., Oceans 123, 5194–5209. https://doi.org/10.1029/2018JC013815.

Marshall, J., Donohoe, A., Ferreira, D., McGee, D., 2014. The ocean's role in setting the mean position of the Inter-Tropical Convergence Zone. Clim. Dyn. 42 (7–8), 1967–1979. https://doi.org/10.1007/s00382-013-1767-z.

Mcintyre, A., Molfino, B., 1996. Forcing of Atlantic equatorial and subpolar millennial cycles by precession. Science 274 (13), 1867–1870.

Mcintyre, A., Ruddiman, W.F., Karlin, K., Mix, A.C., 1989. Surface water response of the equatorial Atlantic Ocean to orbital forcing. Paleoceanography 4 (1), 19–55. https://doi.org/10.1029/PA004i001p00019.

Molfino, B., Mcintyre, A., 1990. Precessional forcing of nutricline dynamics in the equatorial Atlantic. Science 249 (4970), 766–769. https://doi.org/10.1126/science.249.4970.766.

Mulitza, S., Dürkoop, A., Hale, W., Wefer, G., Niebler, H.S., 1997. Planktonic foraminifera as recorders of past surface-water stratification. Geology 25 (4), 335–338. https://doi.org/10.1130/0091-7613(1997)025<0335:PFAROP>2.3.CO;2.

Niemitz, M.D., Billups, K., 2005. Millennial-scale variability in western tropical Atlantic surface ocean hydrography during the early Pliocene. Mar. Micropaleontol. 54 (3–4), 155–166. https://doi.org/10.1016/j.marmicro.2004.10.001.

Poole, R., Tomczak, M., 1999. Optimal multiparameter analysis of the water mass structure in the Atlantic Ocean thermocline. Deep-Sea Res., Part 1, Oceanogr. Res. Pap. 46 (11), 1895–1921. https://doi.org/10.1016/S0967-0637(99)00025-4.

Regenberg, M., Steph, S., Nürnberg, D., Tiedemann, R., Garbe-Schönberg, D., 2009. Calibrating Mg/Ca ratios of multiple planktonic foraminiferal species with δ18O-calcification temperatures: paleothermometry for the upper water column. Earth Planet. Sci. Lett. 278 (3–4), 324–336. https://doi.org/10.1016/j.epsl.2008.12.019.

Reimer, P.J., Bard, E., Bayliss, A., Beck, J.W., Blackwell, P.G., Ramsey, C.B., et al., 2013. IntCal13 and Marine13 radiocarbon age calibration curves 0–50,000 years cal BP. Radiocarbon 55 (04), 1869–1887. https://doi.org/10.2458/azu_js_rc.55.16947.

Rodrigues, R.R., Rothstein, L.M., Wimbush, M., 2007. Seasonal variability of the South Equatorial Current bifurcation in the Atlantic Ocean: a numerical study. J. Phys. Oceanogr. 37 (1), 16–30. https://doi.org/10.1175/JPO2983.1.

Rutherford, S., D'Hondt, S., 2000. Early onset and tropical forcing of 100,000-year Pleistocene glacial cycles. Nature 408, 71–75. https://doi.org/10.1038/35040533.

Santos, T.P., Ballalai, J.M., Franco, D.R., Oliveira, R.R., Lessa, D.O., Venancio, I.M., Chiessi, C.M., Kuhnert, H., Johnstone, H., Albuquerque, A.L.S., 2020. Asymmetric response of the subtropical western South Atlantic thermocline to the Dansgaard-Oeschger events of Marine Isotope Stages 5 and 3. Quat. Sci. Rev. 236. https://doi.org/10.1016/j.quascirev.2020.106307.

Santos, T.P., Lessa, D.O., Venancio, I.M., Chiessi, C.M., Mulitza, S., Kuhnert, H., Govin, A., Machado, T., Costa, K.B., Toledo, F., Dias, B.B., Albuquerque, A.L.S., 2017a. Prolonged warming of the Brazil Current precedes deglaciations. Earth Planet. Sci. Lett. 463, 1–12. https://doi.org/10.1016/j.epsl.2017.01.014.

Santos, T.P., Lessa, D.O., Venancio, I.M., Chiessi, C.M., Mulitza, S., Kuhnert, H., Albuquerque, A.L.S., 2017b. The impact of the AMOC resumption in the western South Atlantic thermocline at the onset of the Last Interglacial. Geophys. Res. Lett. 44. https://doi.org/10.1002/2017GL074457.

Schlitzer, R., 2017. Ocean data view. https://odv.awi.de/.

Schneider, T., Bischoff, T., Haug, G.H., 2014. Migrations and dynamics of the intertropical convergence zone. Nature 513 (7516), 45–53. https://doi.org/10.1038/nature13636.

Schott, F.A., Dengler, M., Zantopp, R., Stramma, L., Fischer, J., Brandt, P., 2005. The shallow and deep western boundary circulation of the South Atlantic at 5°–11°S. J. Phys. Oceanogr. 35, 2031–2053. https://doi.org/10.1175/JPO2813.1.

Schott, F., Fischer, J., Stramma, L., 1998. Transports and pathways of the upper-layer circulation in the western tropical Atlantic. J. Phys. Oceanogr. 28, 1904–1928. https://doi.org/10.1175/1520-0485(1998)028<1904:TAPOTU>2.0.CO;2.

Schulz, M., Mudelsee, M., 2002. REDFIT: estimating red-noise spectra directly from unevenly spaced paleoclimatic time series. Comput. Geosci. 28 (3), 421–426. https://doi.org/10.1016/S0098-3004(01)00044-9.

Scussolini, P., Marino, G., Brummer, G.-J.A., Peeters, F.J.C., 2015. Saline Indian Ocean waters invaded the South Atlantic thermocline during glacial termination II. Geology 43 (2), 139–142. https://doi.org/10.1130/G36238.1.

Shackleton, N.J., 1974. Attainment of isotopic equilibrium between ocean water and the benthonic foraminifera geuns Uvigerina: isotopic changes in the ocean during the last glacial. Colloq. Int. Cent. Natl. Rech. Sci. 219, 203–210.

Skonieczny, C., McGee, D., Winckler, G., Bory, A., Bradtmiller, L.I., Kinsley, C.W., et al., 2019. Monsoon-driven Saharan dust variability over the past 240,000 years. Sci. Adv. 5 (1), 1–9. https://doi.org/10.1126/sciadv.aav1887.

Spratt, R.M., Lisiecki, L.E., 2016. A Late Pleistocene sea level stack. Clim. Past 12 (4), 1079–1092. https://doi.org/10.5194/cp-12-1079-2016.

Sprintall, J., Tomczak, M., 1993. On the formation of Central Water and thermocline ventilation in the southern hemisphere. Deep-Sea Res. 40, 827–848. https://doi.org/10.1016/0967-0637(93)90074-D.

Steele, M., Morley, R., Ermold, W., 2001. PHC: a global ocean hydrography with a high-quality Arctic Ocean. J. Climate 14 (9), 2079–2087. https://doi.org/10.1175/1520-0442(2001)014<2079:PAGOHW>2.0.CO;2.

Stramma, L., 1991. Geostrophic transport of the South Equatorial Current in the Atlantic. J. Mar. Res. 49 (2), 281–294. https://doi.org/10.1357/002224091784995864.

Stramma, L., England, M., 1999. On the water masses and mean circulation of the South Atlantic Ocean. J. Geophys. Res. 104, 20.863–20.883. https://doi.org/10.1029/1999JC900139.

Timmermann, A., Friedrich, T., Timm, O.E., Chikamoto, M.O., Abe-Ouchi, A., Ganopolski, A., 2014. Modeling obliquity and CO2 effects on southern hemisphere climate during the past 408 ka. J. Climate 27 (5), 1863–1875. https://doi.org/10.1175/JCLI-D-13-00311.1.

Toggweiler, J.R., Lea, D.W., 2010. Temperature differences between the hemispheres and ice age climate variability. Paleoceanography 25, 1–14. https://doi.org/10.1029/2009PA001758.

Vellinga, M., Wu, P., 2004. Low-latitude freshwater influence on centennial variability of the Atlantic thermohaline circulation. J. Climate 17 (23), 4498–4511. https://doi.org/10.1175/3219.1.

Venancio, I.M., Mulitza, S., Govin, A., Santos, T.P., Lessa, D.O., Albuquerque, A.L.S., et al., 2018. Millennial- to orbital-scale responses of Western Equatorial Atlantic thermocline depth to changes in the trade wind system since the last interglacial. Paleoceanogr. Paleoclimatol. 33 (12), 1490–1507. https://doi.org/10.1029/2018PA003437.

Wolff, T., Mulitza, S., Rtihlemann, C., Wefer, G., 1999. Response of the tropical Atlantic thermocline to late Quaternary trade wind changes. Paleoceanography 14 (3), 374–383. https://doi.org/10.1029/1999PA900011.

Yang, J., 1999. A linkage between decadal climate variations in the Labrador Sea and the tropical Atlantic Ocean. Geophys. Res. Lett. 26 (8), 1023–1026. https://doi.org/10.1029/1999GL900181.

Zhang, D., Msadek, R., McPhaden, M.J., Delworth, T., 2011. Multidecadal variability of the North Brazil Current and its connection to the Atlantic meridional overturning circulation. J. Geophys. Res. 116 (C4), 1–9. https://doi.org/10.1029/2010jc006812.

Zweng, M.M., Reagan, J.R., Antonov, J.I., Locarnini, R.A., Mishonov, A.V., Boyer, T.P., Garcia, H.E., Baranova, O.K., Johnson, D.R., Seidov, D., Biddle, M.M., 2013. World ocean atlas 2013, volume 2: salinity. In: Levitus, S. (Ed.), A. Mishonov technical ed.. NOAA Atlas NESDIS 74. 39 pp.